Organ-Specific Recommendations for Increasing Temperature-To-Noise Ratio of Magnetic Resonance Thermometry Using Dual-Pathway Sequences at 1.5T, 3T, and 7T during Guidance of Thermal Therapies

Termal Terapilerin Yönlendirilmesinde Çift Yollu Sekanslar Kullanarak Manyetik Rezonans Termometrisinin Sıcaklık-Gürültü Oranını Artırmak için 1.5T, 3T ve 7T'de Organa Özgü Öneriler

Pelin ÇİRİŞ

Akdeniz University, Biomedical Engineering, Antalya, Turkey

Correspondence Address
Yazışma Adresi

Pelin ÇİRİŞ
Akdeniz Üniversitesi, Biyomedikal Mühendisliği, Antalya, Turkey
E-mail: pelinciris@akdeniz.edu.tr

Received \ Geliş tarihi : 21.03.2019
Accepted \ Kabul tarihi : 16.06.2019
Online published : 06.09.2019
Elektronik yayın tarihi

Çiriş P. Organ-specific recommendations for increasing temperature-to-noise ratio of magnetic resonance thermometry using dual-pathway sequences at 1.5T, 3T, and 7T during guidance of thermal therapies. Akd Med J 2020;2:209-18.

Pelin ÇİRİŞ
ORCID ID: 0000-0002-6405-2462

DOI: 10.17954/amj.2019.1936

ABSTRACT

Objective: Thermal therapies provide minimally-invasive alternatives to surgery. Their safety and efficacy require accurate temperature monitoring. Dual-pathway sequences were shown to improve magnetic resonance (MR) thermometry temperature-to-noise-ratio (TNR) using tissue specific parameters at 3T. This study provides expanded guidance for increasing accuracy and speed, across a wider range of tissue types at magnetic field strengths 1.5T, 3T and 7T.

Material and Methods: TNR of a dual-pathway 'Fast-Imaging-with-Steady-state-free-Precession' (FISP)-'inverted-FISP' (PSIF) sequence was compared to a more conventional dual-FISP. Software was validated against analytical solutions, TNR calculations and Monte Carlo simulations. Recommendations were developed for breast glandular tissue and fat, myometrium, endometrium, cervix, liver, prostate, pancreas, spleen, myocardium, optic nerve and spinal cord at 1.5T and 3T; and for gray matter, white matter, kidney medulla and cortex, skeletal muscle, fat, cartilage, bone marrow at 1.5T, 3T, and 7T.

Results: TNR improved using PSIF-FISP: in the kidney, uterus, prostate, spleen, optic nerve and spinal cord at most parameters and fields; in the liver, pancreas, cartilage, skeletal muscle, myocardium, and breast at only short repetition-times (TR); in the brain at 1.5T and 3T across most parameters, but the benefits decreased at 7T; in fat and bone marrow at 1.5T across most parameters, but the benefits decreased at 3T and 7T; and in the cervix at 1.5T at only short TRs, and at 3T with widespread benefits at most parameters. In all cases, PSIF-FISP improved TNR greatly as TR decreased, and slightly as the flip-angle increased.

Conclusion: MR thermometry TNR and speed can increase considerably using dual-pathway sequences with parameters selected based on target tissue and magnetic field strength.

Key Words: Thermal therapies, Magnetic resonance thermometry, Proton resonance frequency shift, Temperature-to-noise-ratio, Simulation and modeling, 'Fast-Imaging-with-Steady-state-free-Precession' (FISP)-'inverted-FISP' (PSIF).

ÖZ

Amaç: Termal tedaviler, cerrahi müdahaleye minimal invaziv alternatifler sağlar. Güvenlik ve etkinlikleri, doğru sıcaklık izleme gerektirir. Manyetik rezonans (MR) termometrisinin sıcaklık/gürültü oranının (TNR), çift yollu sekanslarla 3T manyetik alan değerinde dokuya özgü parametreler kullanılarak artırılabileceği daha önce gösterilmiştir. Bu çalışma, daha fazla dokuda 1.5T, 3T ve 7T manyetik alan güçlerinde, doğruluk ve hız artırabilmek için, kapsamlı öneriler sunar.

Gereç ve Yöntemler: Çift yollu bir 'Kararlı-Hal-Serbest-Devinim-Hızlı-Görüntüleme' (FISP)-'ters FISP'(PSIF) sekansının TNR'si, daha geleneksel bir çift FISP ile karşılaştırıldı. Analitik çözümler,

TNR hesaplamaları ve Monte Carlo simülasyonları ile yazılım doğrulandı. Öneriler, 1.5T ve 3T'de meme glandüler ve yağ dokusu, miyometriyum, endometriyum, serviks, karaciğer, prostat, pankreas, dalak, miyokard, optik sinir ve omurilik; 1.5T, 3T ve 7T'de gri madde, beyaz madde, böbrek medulla ve korteks, iskelet kası, yağ, kıkırdak ve kemik iliği için, geliştirildi.

Bulgular: PSIF-FISP kullanımı, TR azaldıkça TNR'yi büyük ölçüde artırırken, sapma-açısı arttıkça ise TNR'yi hafifçe artırmıştır. Özellikle, böbrek, uterus, prostat, dalak, optik sinir ve omurilikte çoğu parametre ayarında ve alan değerinde iyileşme görülmüştür. Ek olarak, karaciğer, pankreas, kıkırdak, iskelet kası, miyokard ve memede yalnızca kısa tekrar-süresi (TR) ayarlarında iyileşme görülmüştür. Beyinde 1.5T ve 3T'de çoğu parametre ayarlarında iyileşme görülürken, iyileşme 7T'de azalmıştır. Yağ ve kemik iliğinde 1.5T'de çoğu parametre ayarında iyileşme görülürken, iyileşme 3T ve 7T'de azalmıştır. Servikste ise 3T'de çoğu parametre ayarlarında yaygın iyileşme görülürken, 1.5T'de yalnızca kısa TR ayarlarında iyileşme görülmüştür.

Sonuç: MR termometrisi TNR ve görüntü elde etme hızı, çift yollu dizinlerle hedef dokuya ve manyetik alan değerine göre seçilen parametreler kullanılarak, önemli ölçüde artırılabilir.

Anahtar Sözcükler: Termal tedaviler, Manyetik rezonans termometrisi, Proton rezonans frekans kayması, Sıcaklık-gürültü oranı, Simülasyon ve modelleme, Kararlı-Hal-Serbest-Devinim-Hızlı-Görüntüleme' (FISP)-'ters FISP'(PSIF)

INTRODUCTION

Thermal therapies, specifically hyperthermia, such as ablation using radio-frequency (RF), microwave, laser, or focused ultrasound (FUS) devices, offer minimally-invasive alternatives to surgical resection, and provide effective adjuvants to radiation, chemotherapy, and immunotherapy across a wide range of conditions. Promising results have been achieved in the treatment of brain tumors (1), neurological disorders (2), strokes (3), uterine fibroids (4) and bleeding (5), thyroid nodules (6), cancers of the breast (7), pancreas, prostate (8), liver and kidney (9), as well as lung, soft tissue (10) and bone (11), with thermal therapies allowing access to tumors that are more difficult to reach with traditional open surgeries, reducing certain risks associated with traditional open surgeries, shortening recovery times and lessening pain after treatment.

Thermal therapies require maintenance of the target tissue temperature within a narrow range for extended periods of time, thus accurate targeting and temperature monitoring is essential for safe and effective applications. Magnetic resonance (MR) imaging and MR thermometry are natural choices for guiding thermal therapies. MR has excellent soft tissue contrast and can visualize the anatomy for accurate targeting and enable accurate three-dimensional treatment planning. MR can also detect temperature changes in real-time, noninvasively (12), which enables real-time monitoring and guidance to ensure that the desired thermal damage (i.e. tissue denaturation and coagulative necrosis) occurs.

Most commonly, MR thermometry is performed based on the proton-resonant-frequency (PRF) shift of water signals (13, 14). PRF depends on the magnetic field experienced by the protons. Hydrogen electrons shield the nucleus from the magnetic field, decreasing the PRF. Hydrogen electrons are pulled away from their protons by hydrogen bonds between water molecules, increasing the PRF. Tissue temperature increases cause these hydrogen bonds to stretch, bend, and break. As a result, hydrogen electrons shield the nucleus from the magnetic field more, reducing the magnetic field experienced by the protons and the PRF. The effect is the same for all aqueous tissues and linear with temperature within the temperature range of interest, with the PRF shift coefficient of $\alpha = 0.01$ ppm/°C and

$$\Delta T = (\varphi - \varphi_0) / (\alpha \gamma B_0 TE), \quad (1)$$

where $\gamma = 2\pi \times 42.58$ MHz/T is the gyromagnetic ratio for hydrogen, B_0 is the field strength, TE is the echo time, and φ and φ_0 are the heating and reference phases, respectively. After treatment, MRI can also be used for assessment of treatment response and the success of these thermal treatments (i.e. based on the fraction of the target volume that becomes nonperfused following treatment, for instance based on post-contrast-enhanced T1-weighted imaging: when blood vessels are damaged, the contrast agent gadolinium does not reach necrotic tissue and does not increase signal intensity as it does in well-perfused tissue).

MR PRF shift thermometry applications have ranged from RF ablation of cardiac arrhythmias (15), laser-induced interstitial thermal therapy targeting the liver (16), interstitial microwave thermal therapy in the brain (17), FUS sonication of prostate tumors (18), percutaneous laser disc decompression (19), through guiding ultrasound-induced local hyperthermia and drug delivery (20), for FUS heating of the breast (21), transcranial FUS (22), measurement of complex temperature distributions within fluid flow (23), as well as combining MR PRF with acoustic radiation force imaging (24), with many of these applications benefiting from fast imaging and improved coverage without compromising temperature accuracy.

In PRF shift thermometry, tissue temperature is typically quantitatively monitored based on the change in phase, resulting from the temperature-induced PRF shift, using

gradient-recalled echo (GRE) sequences (13, 14). Many different GRE sequences are sensitive to the PRF shift, i.e. spoiled (e.g., spoiled gradient (SPGR), fast low angle shot (FLASH)), unbalanced steady-state (e.g., fast imaging with steady-state free precession (FISP), gradient recalled acquisition in the steady state (GRASS)), balanced steady-state (e.g., balanced-steady state free precession (SSFP), True-FISP, fast imaging employing steady state acquisition (FIESTA), balanced-fast field echo (FFE)). Spoiled sequences are commonly used for PRF thermometry; however, their signal decreases as the repetition time (TR) decreases. In contrast, unbalanced steady-state sequences can maintain high signal levels for effectively capturing the PRF effect even at very short TR settings. Short TR settings can be useful for faster scanning, and thus also improve motion robustness. The two typically-strongest signal pathways in steady-state sequences are maximally sensitive to temperature at different portions of the TR period, with the 'fast imaging with steady-state free precession' (FISP) pathway being maximally sensitive late in TR, and the inverted-FISP (PSIF) pathway being maximally sensitive early in TR. Dual-pathway sequences, a particular type of unbalanced steady-state sequences, rely on this fact and were indeed shown to improve the temperature-to-noise ratio (TNR) over standard GRE sequences (25), with image acquisition parameters recommendations provided across various tissues at 3T (26).

Given that 1.5T is the most widely available option in most clinical settings, and as 7T is becoming more available beyond research settings and entering the clinical arena, further guidance across a wider range of tissues and field-strengths is desirable. In this study, we developed recommendations for increasing MR thermometry TNR, while maintaining high temporal and spatial resolutions, using dual-pathway sequences, across a wider range of tissue types and more field strengths (at 1.5T, 3T and 7T) than previously available, providing guidance regarding preferable parameter settings and corresponding expected TNR improvements.

METHODS

The dual-pathway PSIF-FISP sequence, which samples a PSIF signal in the early portion of the TR period and a FISP signal in the late portion of the TR period (25, 26), was simulated and validated against analytical calculations and Monte Carlo simulations across a number of different contexts. The validated software was used to simulate experiments across a wide range of tissue types, at various field strengths and imaging conditions, leading to our final recommendations on when, where and how to improve TNR using dual-pathways sequences.

A) Simulations

All calculations were performed in Matlab (Mathworks, Natick, MA). A homogeneous 1D object without any k-space features beyond a delta function was simulated with very high spatial resolution. With unbalanced steady-state sequences, while all magnetization pathways were always present, most pathways are displaced to distant regions of k-space where we can ignore them. Numerical simulations allow achieving arbitrarily high spatial resolutions, with arbitrarily-large k-space extent, where a Fourier transform can reveal several distinct pathway signals. Simulated voxels contained isochromats, with a Lorentzian frequency distribution, pointing along the z direction. The simulation involved applying rotation matrices to simulate excitation with RF pulses, the effects of imaging gradients and frequency offsets, as well as T_1 recovery along z, and $T_2=1/R_2$ decay along x and y. RF phase alternated by 180° every TR, and a half-flip angle excitation in the first TR accelerated the approach to steady-state. The first 500 excitations were discarded to ensure that steady-state was reached even for short TR and long T_1 settings. For positive-pathway signals (e.g., FISP), T_2 decay, combined with coherence loss among isochromats led to a $T_2^* = 1/(R_2 + R_2')$ decay. For negative pathways (e.g., PSIF), signals behaved according to $1/(R_2 + R_2')$ as expected (27). The appropriate pathway signals were captured by Fourier transforming the object's signal at every sampling window.

B) Analytical solutions

In the absence of a reversible decay component (i.e., $R_2' = 0$ and $T_2^* = T_2$), PSIF and FISP signal is given by (28-30):

$$S_{PSIF}(TE) = M_0 \tan\left(\frac{\theta}{2}\right)\left(\frac{1-(1-E_1C)\,\mathrm{x}R}{E_2}\right) x\, e^{\frac{TE}{T_2}}, \quad (2)$$

$$S_{FISP}(TE) = M_0 \tan\left(\frac{\theta}{2}\right)(1-(E_1-C)\,x\,R)\,x\,e^{-TE/T_2}, \quad (3)$$

where θ is the flip angle (FA), $C = COS(\theta)$, M_0 is the equilibrium magnetization, $E_1 = e^{-TR/T_1}$, $E_2 = e^{-TR/T_2}$, and R is given by

$$R = \sqrt{(1-E_2^2)/((1-E_1C)^2 - (E_2x(E_1-C))^2)} \quad (4)$$

Simulations and calculations used the parameter ranges: T_1=300 to 2100 ms, T_2=20 to 170 ms, θ=5 to 90°, TR= 5 to 50 ms, with 10 evenly-spaced values in each range, TE_{PSIF}=TR/4 and TE_{FISP}=TR/4. Each parameter was simulated over its whole range, while the remaining parameters were kept constant in the middle of their own

ranges (T_1=1200 ms, T_2=95 ms, θ=47.5°, TR=27.5 ms). 2D slice profiles were simulated using FAs from $\theta = 0^o$ through the prescribed nominal FA setting in steps of 3° combined with Gaussian weighting.

C) TNR equation

The PSIF and FISP signal levels from a variety of tissues and imaging conditions were converted into a measure of TNR, using the dual-FISP sequence as a reference standard, as follows:

The temperature sensitivity for FISP and PSIF signals, L_{FISP} and L_{PSIF}, is (25):

$$\Lambda_{FISP} = \alpha \text{ x } \gamma \text{ x } B_0 \text{ x } TE_{FISP}, \quad (5)$$

$$\Lambda_{PSIF} = \alpha \text{ x } \gamma \text{ x } B_0 \text{ x } (TR - TE_{PSIF}), \quad (6)$$

where phase shifts from either FISP or PSIF signals, $\Delta\phi_{FISP}$ or $\Delta\phi_{PSIF}$, provide the relative temperature:

$$\Delta T_{FISP} = \Delta\phi_{FISP} / \Lambda_{FISP}, \quad (7)$$

$$\Delta T_{PSIF} = \Delta\phi_{PSIF} / \Lambda_{PSIF}, \quad (8)$$

and TNR-optimum estimates are obtained by combining measurements from individual pathways with proper weighting (25):

$$\Delta T_{PSIF-FISP} = \frac{\Delta T_{PSIF} \text{x} W_{PSIF} + \Delta T_{FISP} \text{x} W_{FISP}}{W_{PSIF} + W_{FISP}}, \quad (9)$$

$$\Delta T_{dual-FISP} = \frac{\Delta T_{FISP1} \text{x} W_{FISP1} + \Delta T_{FISP2} \text{x} W_{FISP2}}{W_{FISP1} + W_{FISP2}}, \quad (10)$$

where the weights are:

$$W_{PSIF} = (S_{PSIF} \text{x} \Lambda_{PSIF})^2, \quad (11)$$

$$W_{FISP} = (S_{FISP} \text{x} \Lambda_{FISP})^2, \quad (12)$$

assuming the same noise statistics (i.e., same imaging bandwidth, matrix size, acceleration, scaling) for all FISP and PSIF images.

The relative TNR, E, of the PSIF-FISP sequence, as compared to a dual-FISP sequence, depends only on the weights from Eq. 12, i.e., *E* is independent of the actual temperature change being measured (26):

$$E = \sqrt{\frac{W_{PSIF} + W_{FISP}}{W_{FISP1} + W_{FISP2}}}, \quad (13)$$

E in Eq. 13 compares PSIF-FISP to a dual-FISP as reference for certain image acquisition parameters. In addition, to compare a PSIF-FISP sequence for certain image acquisition parameters to the best possible (i.e., an optimized) dual-FISP sequence, the following version of Eq. 13 is also considered:

$$E_{global} = \frac{\sqrt{W_{PSIF} + W_{FISP}}}{\max\text{imum}\left(\sqrt{W_{FISP1} + W_{FISP2}}\right)}, \quad (14)$$

where the maximum(x) function is applied over all simulated image acquisition parameters.

D) Monte Carlo simulations

Monte Carlo simulations were performed to obtain a Monte Carlo equivalent of *E*, called E_{MC}, to validate Eq. 13. Normally distributed random noise was added to real and imaginary signals from each pathway to generate noisy pre-heating signals. Heat-induced phase shifts were added to simulated pre-heating signals to generate post-heating signals. Finally, normally-distributed random noise was added to both real and imaginary channels of both pre-heating and post-heating signals. Phase differences were divided by the temperature sensitivities given in Eq. 8 to obtain temperature estimates. Relative TNR was obtained by dividing the temperature noise of PSIF-FISP by the temperature noise of dual-FISP:

$$E_{MC} = std(\Delta T_{dual-FISP}) / std(\Delta T_{PSIF-FISP}), \quad (15)$$

E_{MC} and *E* were compared for all combinations of the image acquisition parameters θ = 30°, 45°, 60° and TR = 4, 10, 20 ms, for several tissue types at 1.5T, 3T and 7T, using T_1 and T_2 values as provided in Table I. For all cases, TE_1=TR/4, TE_2=3TR/4, $T_2^* = T_2/2$, and 2D slices were simulated using Gaussian profiles as described.

E) TNR-based recommendations across different field strengths, for various tissue types

Relative TNR, *E* (Eq. 13) was calculated based on simulated PSIF and FISP signals for a wide range of image acquisition parameters (all combinations of θ=3 to 90°, in steps of 3° and TR=2 to 50 ms, in steps of 2 ms) and tissues (Table I).

Regions where the PSIF-FISP sequence improves TNR (*E*>1) vs. reduces TNR (*E*<1), were indicated using color coding: Green represents TNR increases and red represents TNR decreases with PSIF-FISP, while black represents conditions with *E*≈1, where TNR of PSIF-FISP and dual-FISP sequences are nearly equivalent. E_{global}, from Eq. 14, was overlaid onto the color-coded rendering as a contour plot. The resulting display thoroughly compares the TNR performance of PSIF-FISP and dual-FISP sequences, showing where PSIF-FISP performs 'better' in green,

and contour plots indicate how good the performance is, globally.

RESULTS

Figure 1 shows dual-pathway PSIF and FISP signal levels (S/M_0, signal S divided by the equilibrium magnetization M_0) obtained from signal simulations in comparison to those obtained from analytical solutions, as a function of tissue parameters T_1, T_2 and image acquisition parameters θ and TR, with $R_2^{'} = 0$. Dual-pathway simulations agreed very well with analytical solutions from Eq. 2-6 (Figure 1A-D).

Figure 2 provides a comparison of relative TNRs obtained from TNR equations (*E)* vs. TNRs obtained from Monte Carlo experiments (E_{MC}), for all simulated tissue types and various combinations of the imaging parameters FA and TR, across multiple field strengths. Results are displayed in ascending order of relative TNRs at the shortest TR and largest FA setting (TR=4 ms, θ=60°). Excellent agreement was found between the relative TNR *E* (Eq. 13) and the matching Monte Carlo simulation result E_{MC} (Eq. 15) for all simulated tissue types and across multiple field strengths (Figure 2A-C). At 1.5T, the myometrium benefited most from PSIF-FISP among all tested tissues (up to 33% increase), followed closely by endometrium, bone marrow, fat, prostate and kidney tissues (up to 32% increases in all). At 3T, kidney tissues benefited most from PSIF-FISP among all tested tissues (up to 33% increase), followed closely by the cervix and myometrium, optic nerve, prostate and spinal cord (up to 32% increases in all). At 7T, kidney tissues again benefited most from PSIF-FISP among all tested tissues (up to 33% and 32% for medulla and cortex, respectively), followed by brain gray and white matter, bone marrow and fat (up to 30% increases in all). Skeletal muscle consistently benefited least from PSIF-FISP among all tested tissues, across all tested field strengths, however, even in this case, TNR increases up to 25-30% were observed across all field strength depending on the parameter settings. Such close agreement between the simulation software and Monte Carlo simulated data shown in Figure 1A-D, 2A-C provided validation of the simulation approach.

Recommendations for sequence and image acquisition parameters for PRF imaging for various tissue types across multiple field strengths are given in Figure 3. PSIF-FISP improved TNR (green) compared to the more conventional FISP-FISP acquisition in the kidney medulla

Table I: Relaxation rate values, at 1.5T, 3T and 7T, used in simulations.

Tissues	1.5T		3T		7T	
	T_1 (ms)	T_2 (ms)	T_1 (ms)	T_2 (ms)	T_1 (ms)	T_2 (ms)
Brain (Grey Matter)	1197[1]	84[2]	1607[1]	72[2]	1939[1]	47[2]
Brain (White Matter)	646[1]	80[2]	838[1]	71[2]	1126[1]	47[2]
Kidney (Medulla)	1412[3]	85[3]	1676[4]	138[4]	2094[4]	126[4]
Kidney (Cortex)	966[3]	87[3]	1261[4]	121[4]	1661[4]	108[4]
Skeletal Muscle	1130[5]	35[5]	1256[6]	29[6]	1553[6]	23[6]
Fat	288[5]	165[5]	404[6]	48[6]	583[6]	46[6]
Cartilage	1060[5]	42[5]	1016[6]	39[6]	1568[6]	32[6]
Bone Marrow	288[5]	165[5]	381[6]	52[6]	549[6]	47[6]
Breast glandular	1266[7]	58[7]	1445[7]	54[7]		
Breast fat	296[7]	53[7]	367[7]	53[7]		
Uterus Myometrium	1309[3]	117[3]	1514[3]	79[3]		
Uterus Endometrium	1274[3]	101[3]	1453[3]	59[3]		
Uterus Cervix	1135[3]	58[3]	1616[3]	83[3]		
Liver	586[3]	46[3]	809[3]	34[3]		
Prostate	1317[3]	88[3]	1597[3]	74[3]		
Pancreas	584[3]	46[3]	725[3]	43[3]		
Spleen	1057[3]	79[3]	1328[3]	61[3]		
Myocardium	1030[8]	40[8]	1471[8]	47[8]		
Optic Nerve	815[8]	77[8]	1083[8]	78[8]		
Spinal Cord	745[8]	74[8]	993[8]	78[8]		

[1](37), [2](38), [3](39), [4](40), [5](41), [6](42), [7](43), [8](44)

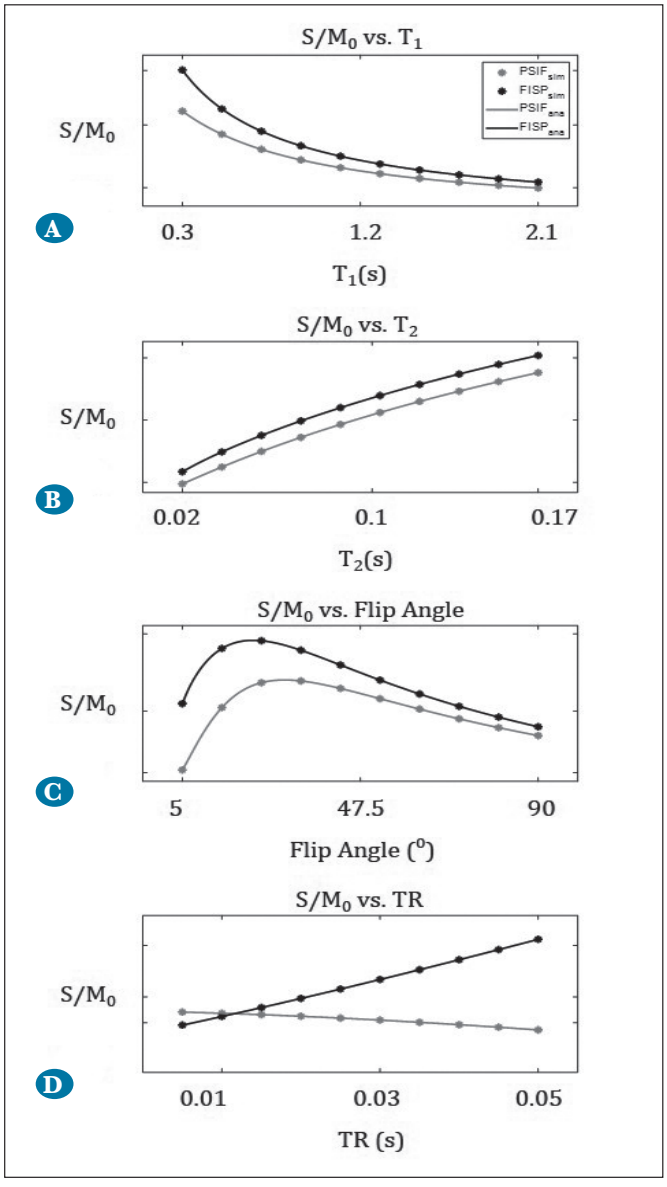

Figure 1: Dual-pathway PSIF and FISP signal simulations and analytical solutions as a function of tissue and image acquisition parameters: T_1, T_2, θ, and TR with $R_2^1 = 0$. **(A)** S/M_0 vs. T_1 (with T_2=95ms, θ=47.5°, TR=27.5ms); **(B)** S/M_0 vs. T_2 (with T_1=1.2 s, θ=47.5°, TR=27.5ms); **(C)** S/M_0 vs. TR (with T_1=1.2 s, T_2=95ms, θ=47.5°); **(D)** S/M_0 vs. θ (with T_1=1.2s, T_2=95 ms, TR=27.5 ms). Simulations and analytical solutions show excellent agreement.

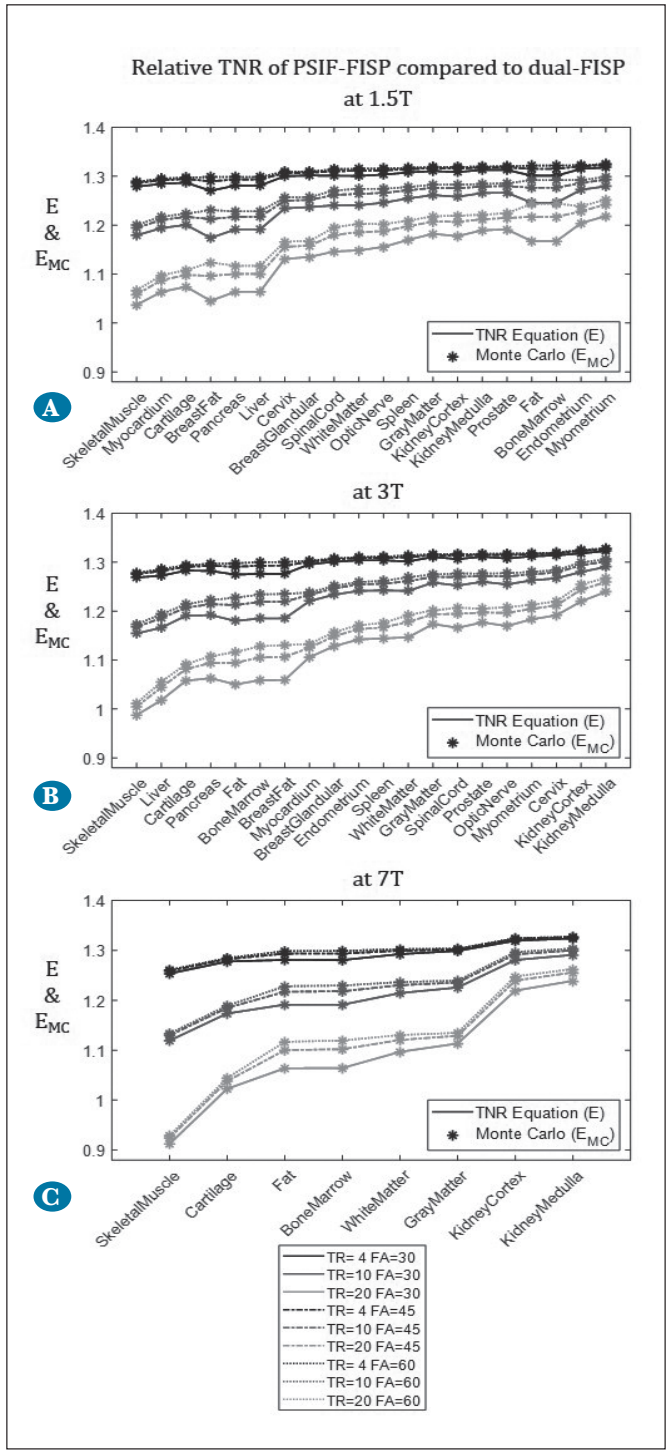

Figure 2: Relative TNRs from TNR equations (E) vs. Monte Carlo experiments (E_{MC}) at **(A)** 1.5T; **(B)** 3T; and **(C)** 7T, for various tissues and image acquisition parameters, also show excellent agreement.

and cortex, uterus, prostate, spleen, optic nerve and spinal cord imaging at most TR and FA settings, as well as field strengths, with benefits increasing at shorter TRs. PSIF-FISP improved TNR only for short TR settings in other tissues such as the liver, pancreas, cartilage, skeletal muscle and specifically myocardium, and breast tissues. PSIF-FISP improved TNR across most parameter settings for brain gray and white matter at 1.5T and 3T field strength, with a considerable reduction in benefit at 7T. PSIF-FISP improved TNR across most parameter settings for fat and bone marrow at 1.5T field strength, with a considerable reduction in benefit at 3T and 7T. On the other hand, PSIF-FISP improved TNR only for short TR settings for the cervix at 1.5T, while the benefit becomes widespread to cover most parameter settings at 3T. In all cases, TNR advantages of PSIF-FISP increased considerably as

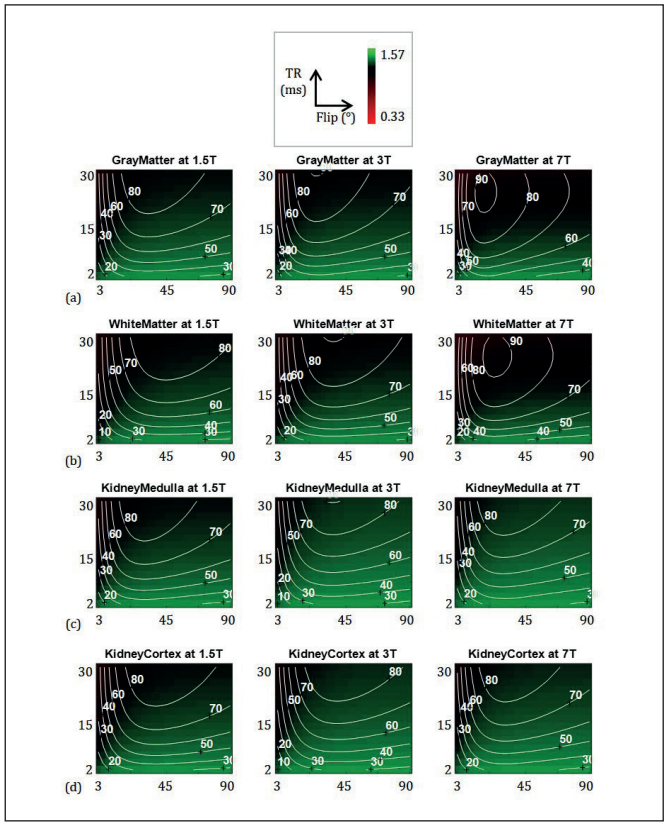

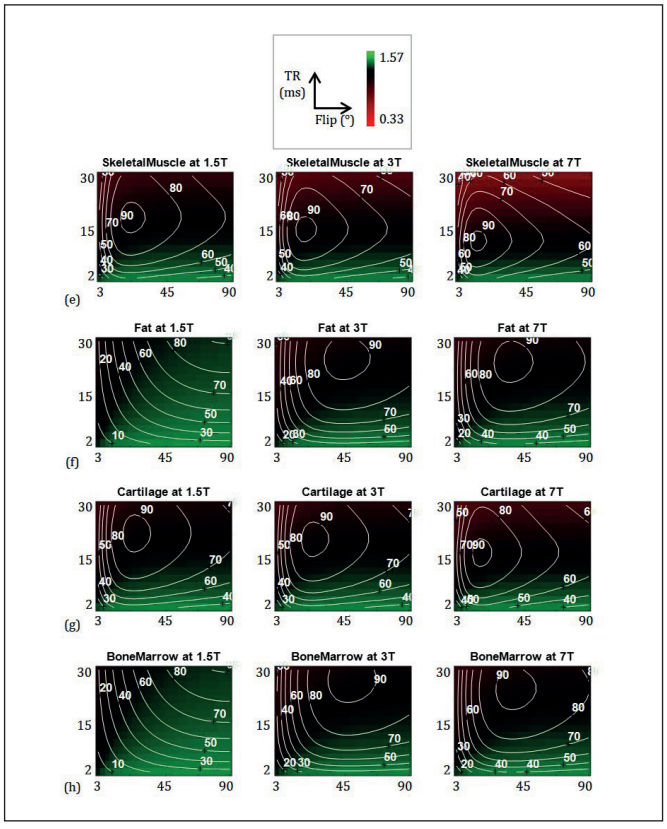

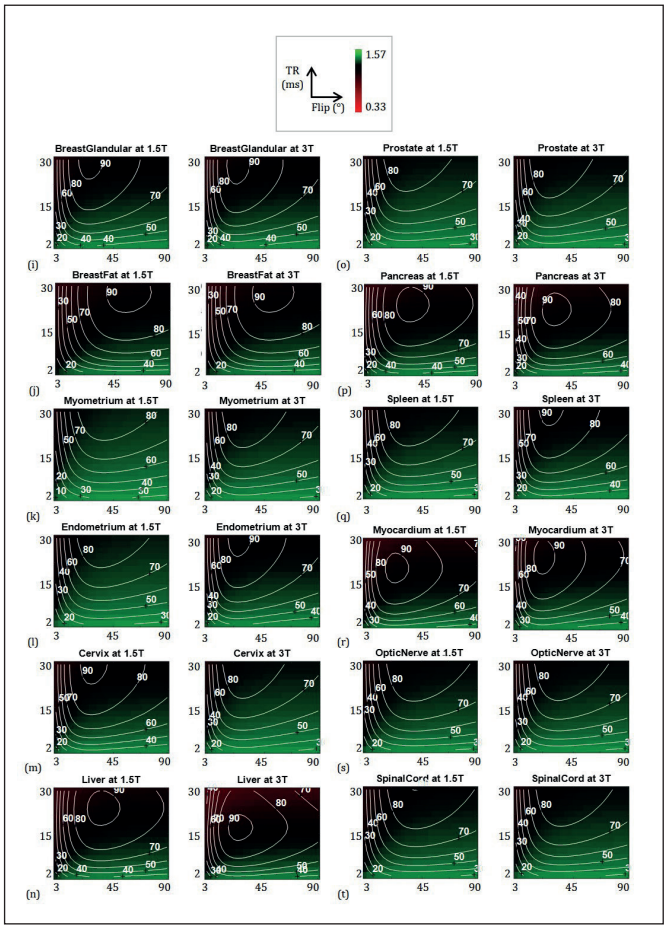

Figure 3: *E*, the relative TNR of PSIF-FISP vs. dual-FISP, for various tissues, field strengths, and acquisition parameters. Green: PSIF-FISP increases TNR. Red: dual-FISP increases TNR (TR increases vertically, FA increases horizontally, the brightest green shade corresponds to 1.57 and the brightest red shade corresponds to 0.33, as also indicated above each figure). Contours: E_{global}, TNR with PSIF-FISP compared to the maximum achievable dual-FISP TNR across all tested parameter sets (as a percentage). (a-h) gray matter, white matter, kidney medulla and cortex, skeletal muscle, fat, cartilage and bone marrow, at 1.5T, 3T, and 7T, respectively; (i-n) breast glandular and fat tissue, myometrium, endometrium, cervix, liver, prostate, pancreas, spleen, myocardium, optic nerve and spinal cord tissues at 1.5T and 3T, respectively.

TR decreased, and slightly as FA increased. Also, TNR increases could be achieved in all tissues using PSIF-FISP, of up to 57% across the tested conditions, depending on the imaging parameter settings.

E_{global} contours in Figure 3 show that tissues where maximal dual-FISP TNR occurred at longer TRs, e.g., >30ms, benefited most from PSIF-FISP. For these cases, a TR could be reduced by a factor of 2-3 using PSIF-FISP for little cost in TNR (Figure 3B-G). On the other hand, tissues where maximal dual-FISP TNR occurred at shorter TR settings benefited least from PSIF-FISP (Figure 3H-N).

In general, tissues with longer T_1 and T_2 values showed a greater tendency to benefit from PSIF-FISP. As tissue heating causes T_1 and T_2 to increase (31-35), the relative TNR would also be expected to increase with heating during thermal therapies.

DISCUSSION

MR imaging and thermometry can improve the safety and efficacy of thermal therapies through targeting and monitoring of temperature, accurately, with high spatial and temporal resolution. Excellent agreement was found between our simulated results, and analytical equations as well as the Monte Carlo approach (Figure 1A-D, 2A-C). Our recommendations for improving MR thermometry TNR, when and where to use dual-pathway sequences, at 1.5T, 3T and 7T, for various tissue types, and quantified expected TNR improvements at various parameter settings (Figure 3) are also in excellent agreement with recommendations previously provided at 3T (26). If low spatial or temporal resolution (or lower geometric fidelity and more artifacts if using an echo-planar readout) are acceptable for a specific application, the dual-FISP sequence may be a better choice since it provides higher TNRs at long TR values. On the other hand, if faster scanning is desirable, the PSIF-FISP sequence may be a better choice since it can improve TNR at short TR values. The PSIF-FISP sequence is TNR advantageous because it samples both the PSIF and FISP components when they are near their maximum temperature sensitivity. The TNR advantage of PSIF-FISP was most prominent in tissues with longer relaxation times, and since relaxation times increase further with temperature (36), the TNR advantages of PSIF-FISP is expected to increase further with heating.

The main limitations of this study are that, despite validations against analytical solutions and Monte Carlo simulations, our recommendations are not based on experiments with each individual tissue and field strength, but rather simulations. Secondly, since T_2* largely also depends on shimming and geometry, rather than being a strict tissue property, it is difficult to be very confident of the accuracy of all tissue T_2* values.

CONCLUSION

In conclusion, organ-specific recommendations for improving TNR of PRF thermometry at various field strengths would help guide the choice of pulse sequence and image acquisition parameters and improve the efficacy and safety of thermal treatments, for a wide range of tissues of interest.

REFERENCES

1. Silva D, Sharma M, Juthani R, Meola A, Barnett GH. Magnetic resonance thermometry and laser interstitial thermal therapy for brain tumors. Neurosurg Clin N Am 2017; 28(4):525-33.
2. Boone CE, Wojtasiewicz T, Moukheiber E, Butala A, Jordao L, Mills KA, Sair H, Anderson WS. MR-Guided functional neurosurgery: Laser ablation and deep brain stimulation. Top Magn Reson Imaging 2018; 27(3):171-7.
3. Zafar A, Quadri SA, Farooqui M, Ortega-Gutierrez S, Hariri OR, Zulfiqar M, Ikram A, Khan MA, Suriya SS, Nunez-Gonzalez JR, Posse S, Mortazavi MM, Yonas H. MRI-Guided high-intensity focused ultrasound as an emerging therapy for stroke: A review. J Neuroimaging 2019; 29(1):5-13.
4. Ierardi AM, Savasi V, Angileri SA, Petrillo M, Sbaraini S, Pinto A, Hanozet F, Marconi AM, Carrafiello G. Percutaneous high frequency microwave ablation of uterine fibroids: Systematic review. Biomed Res Int 2018; 2018:2360107.
5. Kılıç G, Bildacı T, Boruban M. Anormal uterus kanamasında mikrodalga endometriyal ablasyon (Mea) uygulanan hastalarin vaka serisi. Turkish Journal of Gynecologic Oncology 2006; 9(2):39-45.
6. Yang YL, Chen CZ, Zhang XH. Microwave ablation of benign thyroid nodules. Future Oncol 2014; 10(6):1007-14.
7. Mauri G, Sconfienza LM, Pescatori LC, Fedeli MP, Ali M, Di Leo G, Sardanelli F. Technical success, technique efficacy and complications of minimally-invasive imaging-guided percutaneous ablation procedures of breast cancer: A systematic review and meta-analysis. Eur Radiol 2017; 27(8):3199-210.

8. Karadag M, Cecen K, Demir A, Bagcıoğlu M, Kocaaslan R, Sofikerim M. Prostat kanserinde fokal tedavi alternatifleri. Kafkas Tıp Bilimleri Dergisi 2015; 1:18-24.
9. de Senneville BD, Moonen C, Ries M. MRI-Guided HIFU methods for the ablation of liver and renal cancers. Adv Exp Med Biol 2016; 880:43-63.
10. de Baere T, Tselikas L, Gravel G, Hakime A, Deschamps F, Honore C, Mir O, Lecesne A. Interventional radiology: Role in the treatment of sarcomas. Eur J Cancer 2018; 94:148-55.
11. Moynagh MR, Kurup AN, Callstrom MR. Thermal ablation of bone metastases. Semin Intervent Radiol 2018; 35(4):299-308.
12. Parker DL, Smith V, Sheldon P, Crooks LE, Fussell L. Temperature distribution measurements in two-dimensional NMR imaging. Med Phys 1983; 10(3):321-5.
13. Ishihara Y, Calderon A, Watanabe H, Okamoto K, Suzuki Y, Kuroda K, Suzuki Y. A precise and fast temperature mapping using water proton chemical shift. Magn Reson Med 1995; 34(6):814-23.
14. Rieke V, Butts Pauly K. MR thermometry. J Magn Reson Imaging 2008; 27(2):376-90.
15. de Senneville BD, Roujol S, Jais P, Moonen CT, Herigault G, Quesson B. Feasibility of fast MR-thermometry during cardiac radiofrequency ablation. NMR Biomed 2012; 25(4):556-62.
16. Weidensteiner C, Quesson B, Caire-Gana B, Kerioui N, Rullier A, Trillaud H, Moonen CT. Real-time MR temperature mapping of rabbit liver in vivo during thermal ablation. Magn Reson Med 2003; 50(2):322-30.
17. Sherar MD, Moriarty JA, Kolios MC, Chen JC, Peters RD, Ang LC, Hinks RS, Henkelman RM, Bronskill MJ, Kucharcyk W. Comparison of thermal damage calculated using magnetic resonance thermometry, with magnetic resonance imaging post-treatment and histology, after interstitial microwave thermal therapy of rabbit brain. Phys Med Biol 2000; 45(12):3563-76.
18. Smith NB, Buchanan MT, Hynynen K. Transrectal ultrasound applicator for prostate heating monitored using MRI thermometry. Int J Radiat Oncol Biol Phys 1999; 43(1):217-25.
19. Streitparth F, Walter T, Wonneberger U, Schnackenburg B, Philipp CM, Collettini F, Teichgraber UK, Gebauer B. MR guidance and thermometry of percutaneous laser disc decompression in open MRI: An ex vivo study. Cardiovasc Intervent Radiol 2014; 37(3):777-83.
20. Fite BZ, Liu Y, Kruse DE, Caskey CF, Walton JH, Lai CY, Mahakian LM, Larrat B, Dumont E, Ferrara KW. Magnetic resonance thermometry at 7T for real-time monitoring and correction of ultrasound induced mild hyperthermia. PLoS One 2012; 7(4):e35509.
21. Svedin BT, Payne A, Parker DL. Respiration artifact correction in three-dimensional proton resonance frequency MR thermometry using phase navigators. Magn Reson Med 2016; 76(1):206-13.
22. Odeen H, de Bever J, Almquist S, Farrer A, Todd N, Payne A, Snell JW, Christensen DA, Parker DL. Treatment envelope evaluation in transcranial magnetic resonance-guided focused ultrasound utilizing 3D MR thermometry. J Ther Ultrasound 2014; 2:19.
23. Buchenberg WB, Wassermann F, Grundmann S, Jung B, Simpson R. Acquisition of 3D temperature distributions in fluid flow using proton resonance frequency thermometry. Magn Reson Med 2016; 76(1):145-55.
24. de Bever JT, Odeen H, Hofstetter LW, Parker DL. Simultaneous MR thermometry and acoustic radiation force imaging using interleaved acquisition. Magn Reson Med 2018; 79(3):1515-24.
25. Madore B, Panych LP, Mei CS, Yuan J, Chu R. Multipathway sequences for MR thermometry. Magn Reson Med 2011; 66(3):658-68.
26. Ciris PA, Cheng CC, Mei CS, Panych LP, Madore B. Dual-Pathway sequences for MR thermometry: When and where to use them. Magn Reson Med 2017; 77(3):1193-200.
27. Cheng C-C, Mei C-S, Aksit Ciris P, Mulkern RV, Balasubramanian M, Chung H-W, Chao T-C, Panych LP, Madore B. Simultaneous frequency and T2 mapping, applied to thermometry and to susceptibility-weighted imaging. Proceedings of the International Society of Magnetic Resonance in Medicine, 2015. Toronto, Canada. 333.
28. Hanicke W, Vogel HU. An analytical solution for the SSFP signal in MRI. Magn Reson Med 2003; 49(4):771-5.
29. Zur Y, Stokar S, Bendel P. An analysis of fast imaging sequences with steady-state transverse magnetization refocusing. Magn Reson Med 1988; 6(2):175-93.
30. Gyngell ML. The steady-state signals in short-repetition-time sequences. Journal of Magnetic Resonance (1969) 1989; 81(3):474-83.
31. Lewa CJ, Majewska Z. Temperature relationships of proton spin-lattice relaxation time T1 in Biological Tissues. Bull Cancer 1980; 67(5):525-30.
32. Cline HE, Hynynen K, Hardy CJ, Watkins RD, Schenck JF, Jolesz FA. MR temperature mapping of focused ultrasound surgery. Magn Reson Med 1994; 31(6):628-36.
33. Matsumoto R, Oshio K, Jolesz FA. Monitoring of laser and freezing-induced ablation in the liver with T1-weighted MR imaging. J Magn Reson Imaging 1992; 2(5):555-62.

34. Graham SJ, Bronskill MJ, Henkelman RM. Time and temperature dependence of MR parameters during thermal coagulation of ex vivo rabbit muscle. Magn Reson Med 1998; 39(2):198-203.
35. Bazrafshan B, Hübner F, Farshid P, Larson MC, Vogel V, Mäntele W, Vogl TJ. A liver-mimicking MRI phantom for thermal ablation experiments. Medical Physics 2011; 38(5):2674.
36. Bottomley PA, Foster TH, Argersinger RE, Pfeifer LM. A review of normal tissue hydrogen NMR relaxation times and relaxation mechanisms from 1-100 MHz: dependence on tissue type, NMR frequency, temperature, species, excision, and age. Med Phys 1984; 11(4):425-48.
37. Wright PJ, Mougin OE, Totman JJ, Peters AM, Brookes MJ, Coxon R, Morris PE, Clemence M, Francis ST, Bowtell RW, Gowland PA. Water proton T1 measurements in brain tissue at 7, 3, and 1.5 T using IR-EPI, IR-TSE, and MPRAGE: Results and optimization. MAGMA 2008; 21(1-2):121-30.
38. Cox RW, Gowland PA. Measuring T2 and T2' in the brain at 1.5T, 3T and 7T using a hybrid gradient echo-spin echo sequence and EPI. Toronto: International Society for Magnetic Resonance in Medicine, 2008.
39. de Bazelaire CM, G. D, Rofsky NM, Alsop DC. MR imaging relaxation times of abdominal and pelvic tissues measured in vivo at 3.0 T: Preliminary results. Radiology 2004; 230(3):652-9.
40. Metzger GJ, Snyder C, Akgun C, Vaughan T, Ugurbil K, Van de Moortele PF. Local B1+ shimming for prostate imaging with transceiver arrays at 7T based on subject-dependent transmit phase measurements. Magn Reson Med 2008; 59(2):396-409.
41. Gold GE, Han E, Stainsby J, Wright G, Brittain J, Beaulieu C. Musculoskeletal MRI at 3.0 T: Relaxation times and image contrast. AJR Am J Roentgenol 2004; 183(2):343-51.
42. Jordan CD, Saranathan M, Bangerter NK, Hargreaves BA, Gold GE. Musculoskeletal MRI at 3.0 T and 7.0 T: A comparison of relaxation times and image contrast. Eur J Radiol 2013; 82(5):734-9.
43. Rakow-Penner R, Daniel B, Yu H, Sawyer-Glover A, Glover GH. Relaxation times of breast tissue at 1.5T and 3T measured using IDEAL. J Magn Reson Imaging 2006; 23(1):87-91.
44. Stanisz GJ, Odrobina EE, Pun J, Escaravage M, Graham SJ, Bronskill MJ, Henkelman RM. T1, T2 relaxation and magnetization transfer in tissue at 3T. Magn Reson Med 2005; 54(3):507-12.